2009

Dynamic path selection along branched faults: Experiments involving sub-Rayleigh and supershear ruptures

Carl-Ernst Rousseau
University of Rhode Island, roussce@uri.edu

Ares J. Rosakis

Citation/Publisher Attribution
Rousseau, C.-E., & A. J. Rosakis. (2009). Dynamic path selection along branched faults: Experiments involving sub-Rayleigh and supershear ruptures, *J. Geophys. Res.*, 114, B08303, doi: 10.1029/2008JB006173.
Available at: https://doi.org/10.1029/2008JB006173

Dynamic path selection along branched faults: Experiments involving sub-Rayleigh and supershear ruptures

Carl-Ernst Rousseau[1] and Ares J. Rosakis[2]

Received 27 October 2008; revised 12 March 2009; accepted 12 May 2009; published 13 August 2009.

[1] Building upon previous laboratory earthquake experiments of dynamic shear rupture growth taking place along faults with simple kinks, new and complex fault geometries involving cohesively held fault branches are studied. Asymmetric impact at the specimen boundaries controls the incoming shear ruptures, which are manipulated to propagate at either sub-Rayleigh or supershear velocities. High-speed photography and dynamic photoelasticity are used with a model material, Homalite-100, to monitor incoming and outgoing rupture propagation, acceleration, deceleration, or arrest at the vicinity of the branch location. Differences and similarities of rupture velocity history between cases involving faults with either simple kinks or branches, on the one hand, and sub-Rayleigh and supershear incoming ruptures, on the other, are highlighted and explained. Results of the experiments show a clear general bias toward large branch inclination, smaller branch angles appearing to be overshadowed and suppressed by the stress field associated with the main fault. Of great interest, also, is the sustenance of rupture propagation along a branch by the Mach cone, when the initial rupture is supershear driven. Generally, higher rupture speeds favors larger arrays of branching angles to be triggered. A companion analysis by Templeton et al. (2009) featuring detailed numerical simulations of these experiments provides further insight into the observed phenomena.

Citation: Rousseau, C.-E., and A. J. Rosakis (2009), Dynamic path selection along branched faults: Experiments involving sub-Rayleigh and supershear ruptures, *J. Geophys. Res.*, *114*, B08303, doi:10.1029/2008JB006173.

1. Introduction

[2] Dynamic interfacial fracture is generally identified as one of the primary causes of failure in welded, bonded, or otherwise joined structures that are subjected to impulse loading. The dynamic fracture theories, which are developed for the study of such engineering structures and are validated in the laboratory level can, in principle, be transferred to much larger scales pertaining to natural earthquake events. Such events are indeed caused by dynamic ruptures, which propagate at very high speeds along preexisting, weak, frictional interfaces in the form of geological faults.

[3] Direct transference of engineering fracture mechanics principles to fault rupture analysis is, however, not always straightforward. In geological faults, the presence of bends, jogs, branches, highly inhomogeneous fault strength and other geometrical complexities, as well as the effects of frictional dissipation complicate the problem. As a result, classical dynamic fracture mechanics theories must be extended [*Rice*, 1980, 2001] and laboratory scale experiments must be modified [*Rosakis*, 2002; *Rosakis et al.*, 2007] in order to accurately represent the evolution of rupture history during earthquake events.

[4] The effect of fault structure complexities on rupture growth history has long been known to structural geologists who have debated the role of such features in exercising control over earthquake ruptures velocity. For instance, and in relation to fault strength inhomogeneities, *Husseini et al.* [1975] have proposed that weak sections of faults are a cause of rupture arrest, whereas *Aki* [1979] has argued that strong sections cause arrest. In relation to fault geometry, *King and Nabelek* [1985] have noted the apparent confinement of earthquakes to region between fault bends, and in a few cases, have isolated their nucleation to the immediate vicinity of bends or jogs. Earthquake events quoted in support of their assertions include the Luhuo, China, (1973), Lice, Turkey (1975), Tangshan, China (1976), and Coyote Lake, California (1979) earthquakes. Likewise, noting that earthquakes appear to repeatedly confine themselves within restricted regions of similar lengths, *Sibson* [1985, 1986] speculated on the presence of local structures that promote both their nucleation and termination. His analysis thus shows fault jogs to be pivotal in the determination of the size of earthquakes.

[5] The direct effect of branches and steps on the extent to which earthquake ruptures are able to propagate has been recognized by, for example, *Wallace* [1970], *Segall and Pollard* [1980], *Barka and Kadinsky-Cade* [1988], and *Harris et al.* [1991]. Further indications of an apparent

[1]Department of Mechanical Engineering, University of Rhode Island, Kingston, Rhode Island, USA.
[2]Graduate Aeronautical Laboratories, California Institute of Technology, Pasadena, California, USA.

0148-0227/09/2008JB006173$09.00

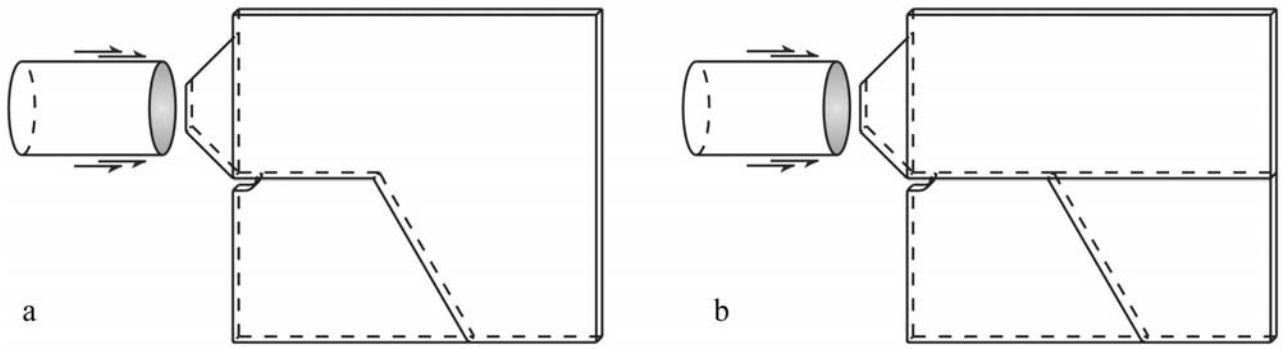

Figure 1. Schematic of specimen geometries: (a) specimen with simple bend beyond the junction and (b) specimen with branched, dual paths beyond the junction.

correlation between fault discontinuities and tectonic disturbances were noted by *Ji et al.* [2000], who spotted signs of rupture deceleration at fault offsets and bends associated with the 1999 Chi-Chi, Taiwan earthquake. Equally persuasive, were similar observations of *Wald and Heaton* [1994] pertaining to the 1992 Landers, California event.

[6] Far more intricate, and as prevalent as jogs, are en echelon faults. Ruptures have been frequently observed to elude the obstacles they pose, by jumping across several fault segments during a single earthquake. *Segall and Du* [1993] have documented this phenomenon during the 1966 Parkfield, California, earthquake. In addition, the 1992 Landers earthquake progressed through two step overs [*Sowers et al.*, 1994; *Zachariasen and Sieh*, 1995]. Also, the Karadere bend (kink) of the North Anatolian fault was unable to stop the 1999 Izmit earthquake [*Harris et al.*, 2002]. To understand such occurrences, *Harris et al.* [1991] and *Harris and Day* [1993, 1999] performed finite difference computations to assess the evolution of spontaneously propagating earthquakes in the vicinity of en echelon faults. Generally, they found the crossing of step overs in excess of 5 km to be prohibitive, whereas narrower ones were easier to overcome.

[7] The role of a change in fault strike during single and repeated earthquake ruptures was first studied by *Aochi et al.* [2000], *Duan and Oglesby* [2005], and *Ando and Yamashita* [2007]. More recently, *Poliakov et al.* [2002], *Kame et al.* [2003], *Bhat et al.* [2004, 2007], and *Duan and Oglesby* [2007] used appropriately modified dynamic fracture methodologies to formulate criteria for branching. More specifically a slip-weakening shear rupture model was used by *Poliakov et al.* [2002] to study the dynamic stress field surrounding a dynamic shear rupture propagating along a predetermined bent path in an elastic solid. They found that rupture nucleation along a preexisting branch was a function of the preexisting stress field, as well as the rupture velocity at the junction. The work by *Poliakov et al.* [2002] was further extended by *Kame et al.* [2003], *Bhat et al.* [2004], and *Fliss et al.* [2005] to investigate how rupture velocity and branch angle affect branching with an emphasis of explaining branch rupture activation during large earthquakes such as the 1992 Landers and the 2002 Denali earthquake events.

[8] Motivated by such theoretical and numerical works, *Rousseau and Rosakis* [2003] initiated experimental studies of fault bends from which they developed models to describe the behavior of a propagating rupture as it travels along a non planar path. These experiments featured incoming shear ruptures propagating at various speeds along cohesively bonded interfaces. For both sub-Rayleigh and supershear incoming ruptures they confirmed that a strong interaction exists between rupture speed, the inclination angle of a bend and its readiness to undergo activation. Subsequent experiments by *Biegel et al.* [2007] investigated the effect of short branches on rupture speed history. These experiments fall under the general umbrella of laboratory studies whose purpose is to mimic earthquake processes [*Xia et al.*, 2004, 2005]. A review of such studies concentrating on the investigation of rupture mode and speed selection during ''laboratory earthquake'' events hosted along frictionally held or cohesive interfaces is given by *Rosakis et al.* [2007].

[9] The same techniques and methodologies adopted by *Rousseau and Rosakis* [2003] are used in this work, in an attempt to shed light onto another condition which is common to crustal faults, namely, the intersection of two planar paths, commonly referred to in this text as branches. The following sections detail our effort to observe and isolate the various phenomena that occur in the immediate vicinity of such junctions. A companion study by *Templeton et al.* [2009] models the experiments in great detail, enables confirmation of the observed phenomena and thus facilitates a thorough analysis of their causes.

2. Specimen and Material Description

[10] The geometry and loading configuration of the specimens tested are such that a mode II crack, or shear rupture, initiates along a horizontal path that extends from one edge of the specimen to the opposite one. Halfway along its length, the horizontal path is intersected by a secondary path inclined at an arbitrary angle with respect to the former. Furthermore, the secondary path is not allowed to cross and extend beyond its intersection with the main, horizontal path. Figure 1b presents a schematic of a specimen just prior to its being loaded. For reference, Figure 1a is also included and corresponds to the case of a horizontal path swerving onto a simple bend (not studied here), to which reference will be made, later on, for comparison purposes.

[11] Several experiments are performed and focus on conditions similar to those of young faults, for which, materials on either sides of the fault have very similar, or

identical elastic properties. The work first concentrates on conditions where the initial (prior to bends or branches) rupture velocity approaches the Rayleigh wave speed (c_R) of the material. Indeed field observations seem to confine the rupture velocities of most earthquakes to the range between $0.76c_R$ and $0.98c_R$ [*Kanamori*, 1994]. However, recent reports have also surfaced indicating that the behavior of certain earthquakes can be better explained, if the rupture velocity resided within the supershear range. Such examples include the 1979 Imperial Valley [*Archuleta*, 1984; *Spudich and Cranswick*, 1984], 1991 Izmit [*Bouchon et al.*, 2000, 2001], 2001 Kunlun [*Bouchon and Vallée*, 2003; *Robinson et al.*, 2006; *Vallée et al.*, 2008], and 2002 Denali [*Ellsworth et al.*, 2004; *Dunham and Archuleta*, 2004; *Aagaard and Heaton*, 2004; *Bouchon and Karabulut*, 2008] earthquakes. Consequently, experiments were also undertaken with initial rupture velocities confined to the range between the shear wave speed, or *S* wave (c_s), and the longitudinal wave speed, or *P* wave (c_l) of the material. For that reason, the optical method of photoelasticity is chosen as a measurement tool because of its exceptional ability to display the shear shock waves, which are essential features of supershear ($c_s < v < c_l$) crack growth [*Rosakis et al.*, 1999; *Rosakis*, 2002; *Rosakis et al.*, 2007].

[12] The experiments are recorded using high-speed photography. The specimens are illuminated by the 100 mm beam of an argon-ion laser, with wavelength $\lambda = 514.5$ nm. The specimens were made of Homalite-100, a polymer which, at room temperature, exhibits both very brittle and linear elastic characteristics. Homalite-100 was used primarily because of its high birefringence, corresponding to a fringe constant of 22.6 KN/m for the green light of the argon-ion laser. Other relevant dynamic material properties include: Young's modulus, $E = 5.2$ GPa, shear modulus, $\mu = 1.9$ GPa, Poisson's ratio, $\nu = 0.34$, and density, $\rho = 1230$ Kg/m^3. Longitudinal wave speed ($c_l = 2295$ m/s), shear wave speed ($c_s = 1310$ m/s), and Rayleigh wave speed ($c_R = 1205$ m/s) were determined directly by impacting a specimen, and monitoring the progression of the compressive stress wavefronts through a photoelastic setup. The material properties and wave speeds indicated correspond to strain rates in excess of 10^3 s^{-1}.

[13] Once assembled, all the specimens were 4.76 mm thick, 178 mm high, and 197 mm long. The narrowness of the specimens, relative to other spatial dimensions, ensures the prevalence of two dimensional, generalized plane stress conditions. Fault lines were simulated by establishing weakened preferential paths through the specimens. First a horizontal path was machined starting from the left edge of the specimen, over a distance of 76 mm. The specimen was then repositioned such as to generate a new path that continued from and was inclined with respect to the previously generated horizontal path. Machining of the incline proceeded until the closest edge of the specimen was reached. The various sections of the specimen were then bonded with a polyester resin solution designed to ensure weaker interfacial fracture properties with respect to the bulk material. The weaker adhesive joint has the effect of trapping the moving crack to the prescribed interface, compelling it to retain its originally imposed mode II state. The elastic properties and density of the polyester resin mixture were very similar to those of the bulk Homalite, except for lower strength and fracture toughness. Mechanical testing of the polyester resin shows the latter two properties to both vary between 30% and 60% of those of Homalite, respectively. The tensile strength of bulk Homalite is 35 MPa, its shear strength, 40 MPa, and its fracture toughness is, 1.6 MPa$\sqrt{}$m.

[14] The resulting specimen was not monolithic, but can be considered to be constitutively homogeneous. Indeed, the existence of a path of lower fracture toughness makes these specimens fracturewise inhomogeneous but does not, in any sense, affect their continuum mechanics description. This is also the condition that prevails across young earthquake faults, which are essentially preferential paths of lower toughness relative to the Earth's crust that trap ruptures, compelling them to proceed only along their prescribed routes [*Rosakis*, 2002].

[15] At the left edge of the material, along the lower side of the interface, a 13 mm long and 1 mm wide starter notch was also machined. A generous radius was placed at its end, as seen in Figure 1, to avoid stress concentrations that might result in superfluous and unwanted crack propagations into the material, with potential for corrupting the experimental results. The purpose of the notch was to prevent the immediate transmission of the incoming impact stress waves (applied at the top) to the bottom half. This in turn guaranteed a relatively flawless mode II initiation loading of the notch tip without disturbances from potential notch face contact.

[16] Finally, the bend location with respect to the left edge of the plate allowed the incoming crack to establish a steady state velocity before reaching the bend site, thereby ensuring uniform conditions at the intersection of the various paths. Also, the location of the bend or the branch was equally remote from the right edge. The specimens were thus designed such that reflected longitudinal waves returning from that edge would not reach the location of the bend until the crack would have moved through the major portion of the horizontal or alternate paths, well beyond the experimental field of observation.

[17] In the sub-Rayleigh regime specimens with secondary faults at angles, α, of $-10°$, $-35°$, $-56°$, and $-80°$, on the extensional side, and angles α, of 10°, and 35°, on the compressional side, were successfully tested. In the supershear regime, successful experiments were undertaken for secondary incline angles, $\alpha = -10°$, $-35°$, $-45°$, $-56°$, $-80°$, and $-100°$, on the extensional side, and $\alpha = 10°$, 35°, 45°, 56°, and 80° on the compressional side. Note that the relative scarcity of experiments in the sub-Rayleigh regime compared to the supershear one is a consequence of the difficulty of experimentally obtaining mode II ruptures running at velocities below c_R. This is to be expected in light of the slip-weakening theoretical predictions of *Burridge et al.* [1979] and the velocity-weakening predictions of *Samudrala et al.* [2002] and *Rosakis* [2002], who have determined that region to be highly unstable. A schematic of the loading mechanism is also displayed in Figure 1.

3. Experimental Apparatus

[18] A detailed schematic illustration of the experimental apparatus is shown in Figure 2. The drawing contains

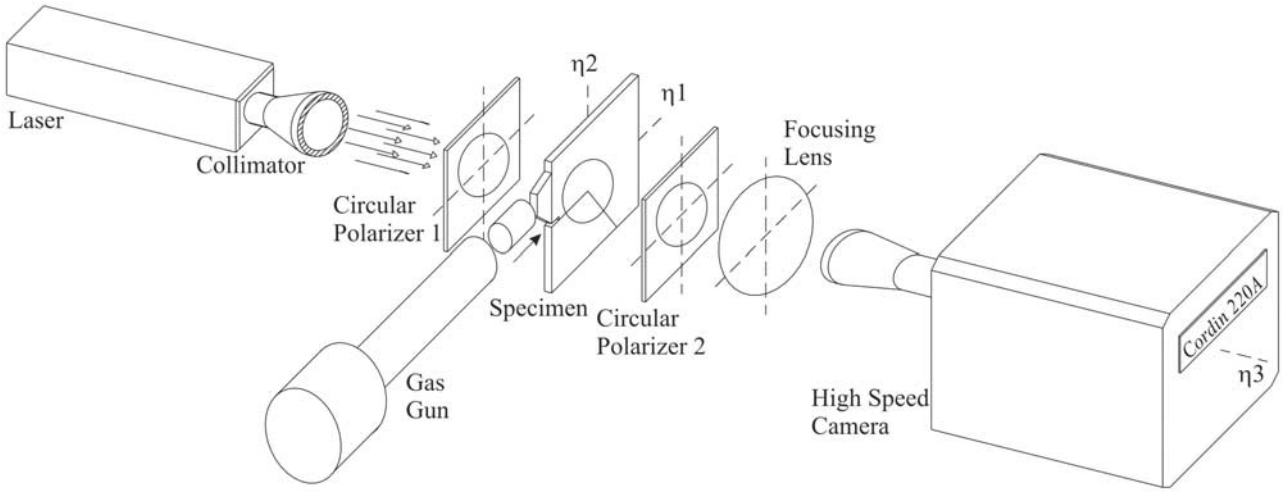

Figure 2. The dynamic photoelastic setup showing a specimen placed within two circular polariscopes and being subjected to impact shear loading by a projectile fired from a high-speed gas gun. The resulting isochromatic fringe patterns are recorded by high-speed photography.

essential elements of the dynamic photoelastic setup. It consists of a steady 100 mm diameter collimated beam generated by an argon-ion continuous laser that traverses a circular polarizer, the specimen, and a second circular polarizer, or analyzer. Disturbances to the coherent beam due to the optical anisotropy of the specimen, as a result of its being stressed, are collected by a 1000 mm lens and directed to the iris of a digital high-speed Cordin camera capable of recording 16 sequential images up to a rate of 100 million frames per second. The high optical sampling rate of the data provides the necessary resolution for measurement of crack velocities within both speed regimes. As the specimen is viewed through the analyzer, isochromatic fringes appear, assuming shades of dark and light (see Figure 3) that can be directly related to the stress level at any point in the specimen. The locations where light is fully revealed (white) correlate to 1/2 fringe orders ($N = 1/2$, $1-1/2$, $2-1/2$, ...), whereas those where light is fully extinguished (black) indicate integer values of N, (0, 1, 2, ...), or full fringe orders. Thus, the magnitude of maximum in-plane shear stresses in the material is given by the following relation [*Dally and Riley*, 1991]:

$$\sigma_1 - \sigma_2 = \frac{F_\sigma}{h} N. \tag{1}$$

In the equation, F_σ is the material fringe constant (22.6 kN/m), h is the material thickness (4.76 mm), N is the fringe order, and σ_1 and σ_2 are the in-plane principal stresses.

[19] Impact of a steel buffer, bonded to the top half of the specimen, generated compressive stress loading waves that are later transmitted into the bulk material as planar waves. The impacting cylindrical projectile was made of hardened steel, with dimensions of 76 mm in length, and 51 mm in diameter. An air pressurized gas gun provided the necessary energy to propel the projectile at speeds ranging from 8 m/s to 40 m/s, depending on the pressure in the barrel. The planar compressive wavefront generated in the material loaded the notch tip and generated an interfacial shear crack. A strain gauge attached to the steel buffer, upon being impacted, triggers the camera to begin recording the event.

4. Experimental Observations: Fringe Progression

[20] The specimens and loading apparatus were designed such as to initiate an interfacial shear crack or rupture,

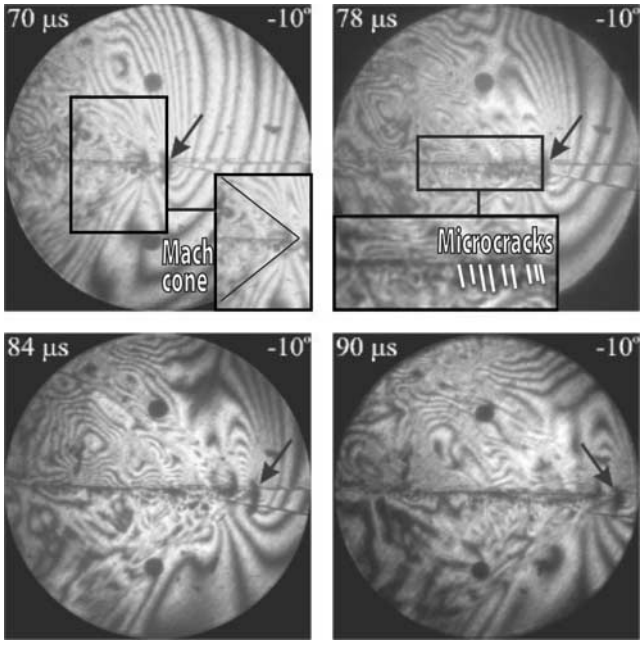

Figure 3. Isochromatic fringe pattern surrounding a mode II crack propagating at supershear speed along a weak plane in Homalite-100. Upon reaching the junction with the extension of the horizontal path and a -10° incline, the crack elects to continue propagating along the horizontal path. Times after impact are 70 μs, 78 μs, 84 μs, and 90 μs. Arrows indicate location of rupture tip.

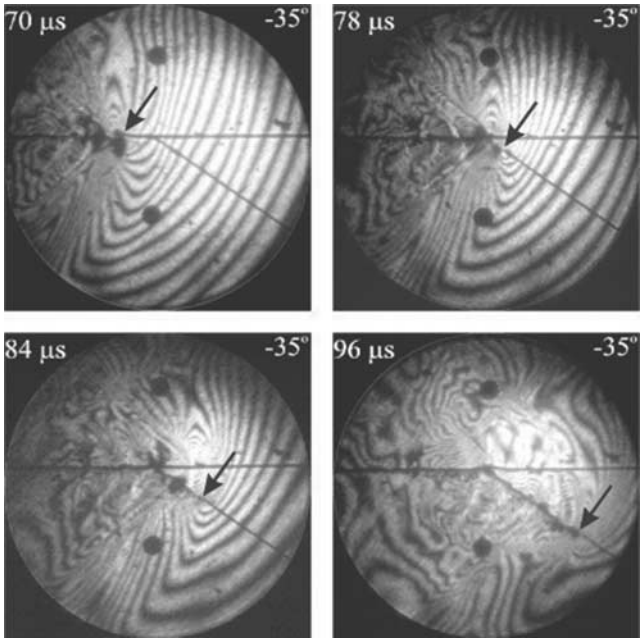

Figure 4. Isochromatic fringe pattern around a mode II crack propagating at supershear speed along a weak plane in Homalite-100. Upon reaching the junction with the extension of the horizontal path and a -35° incline, the crack elects to continue propagating along the inclined path. Times after impact are 70 μs, 78 μs, 84 μs, and 96 μs. Arrows indicate location of rupture tip.

propagating along the weak paths provided, starting at the preexisting notch, shortly after impact (see Figure 1). The impacting steel projectile was released from the gas gun at the constant and repeatable speeds of 20 m/s and 30 m/s, for the sub-Rayleigh and supershear cases, respectively. Within each regime, this ensured relatively consistent levels of crack tip velocity between specimens, as the bends or branched junctions were being approached by the advancing rupture. A coordinate system (x, y) is defined at the tip of the preexisting notch. Along the initial crack path, let a moving coordinate system (η_1, η_2) be present and follow the advancing rupture. The moving coordinate system is thus related to the stationary one as $\eta_1 = x - \int_0^t v(t')dt'$, and $\eta_2 = y$. Also, angular conventions are such that positive angles are defined counterclockwise with respect to the direction of crack motion, whereas negative angles are in the clockwise direction. All images taken were centered at the starting location of the branch, with a field of view having a diameter of 100 mm (see Figure 3). Two small circular black dots located on either side of the initial crack path can be observed at the location corresponding to the beginning of the secondary path, and were used for reference and scaling.

[21] A sequence of four interferograms is first shown in Figure 3. It depicts a case where the horizontal path is accompanied by a secondary path oriented downward, at an angle $\alpha = -10^\circ$ (extensional side). In each frame, an arrow points to the instantaneous location of the rupture tip. The first frame is recorded at time $t = 70$ μs following impact of the specimen by the projectile. On the right side of the image, the initial, impact-induced compressive waves are seen propagating to the right, though exhibiting a slight downward tilt. These waves preload the specimen, establishing a stress field wherein a relatively large, compressive component, σ_{xx}, exists along the main path, while a much smaller compressive stress, σ_{yy}, provides a very modest aid to the bonded interface.

[22] On the left side of the image, there exists a triangular wedge that defines a discontinuity in the fringe pattern. It is a Mach cone, which confirms the supershear nature of the rupture with respect of the shear or S wave, c_s. The Mach cone also serves in determining the rupture velocity, which is defined as $v = c_s/\sin(\psi)$, ψ being the angle either line of discontinuity of the Mach cone forms with the direction of crack motion. Both edges of the cone, as well as the outgoing compressive fringes, come together at a visible stress concentration point corresponding to the rupture tip. In the present frame, the latter is located slightly before the intersection of the two paths.

[23] Also present in the frame are opening microcracks, prominently emphasized in the insert, developing in real time below the rupturing interface. They are elongated further in the subsequent frames where they become more prominent. These secondary tensile cracks were observed in all the experiments conducted. An analysis describing the mechanism guiding their formation is given by *Samudrala et al.* [2002] and their possible connection to pseudotachylite injection veins observed in exhumed faults was discussed by *Rosakis* [2002]. In Figure 3, however, they experience a premature demise shortly after initiation, very near the interface, thus disallowing formation of the large shadow spots usually associated with their mode I crack tips.

[24] The progress of the rupture at 78 μs, then 84 μs is more difficult to interpret, as the dark spot, or caustics, corresponding to the rupture tip stress concentration seems to encompass both paths. It must be noted that these caustics are also representative of regions where the resolution of the experimental method is being taxed by extreme levels of specimen deformation that cannot be interpreted numerically. In this present case, mere caustics, and not rupture is being tracked, as postmortem examination of four specimens with this identical configuration all confirmed the bent interface to still be firmly bonded and seemingly unaffected by the incoming rupture. This is also corroborated by observation of the microcracks, which continue growing along the extension of the horizontal path while being absent from the inclined path. Finally, the last frame recorded at 90 μs shows more clearly that the rupture is indeed confined to the upper, main fault. In the last three images, the progression of the rupture is always accompanied by Mach cones that have angles of similar magnitudes to that of the mach cone preceding the central branching location. Therefore, the rupture continues along a straight line and seems to proceed unaltered beyond the branch.

[25] Figure 4 is representative of an entirely different type of behavior. In this case, also featuring dual paths beyond the junction, the secondary fault is inclined -35° downward, toward the extensional side of the specimen. At 70 μs, the rupture has not yet arrived at the intersection of the three weakened paths provided. The image displays the usual characteristics, i.e., the Mach cone traveling away from the

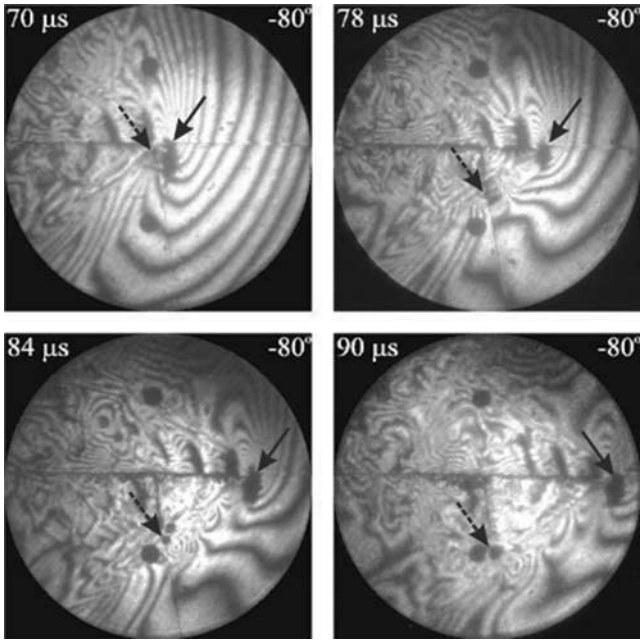

Figure 5. Isochromatic fringe pattern around a mode II crack propagating at supershear speed along a weak plane in Homalite-100. Beyond the junction with the extension of the horizontal path and a $-80°$ incline, the crack simultaneously propagates along both paths. Times after impact are 70 μs, 78 μs, 84 μs, and 90 μs. Arrows indicate location of rupture tip.

impact point while attached to the rupture tip, and to the right of the image, the slightly downward slanted compression stress waves. At 78 μs, the rupture has just overshot the junction and is preparing its journey downward along the incline. At this point, the Mach cone seems to dissociate from the incoming rupture tip, and keeps moving along the horizontal direction, although the rupture has now clearly turned onto the incline. This and subsequent tests of identical configuration could not clearly point to any attempt of the rupture at engaging onto the horizontal interface beyond the intersection point. At 84 μs following impact, the rupture is well on its way along the secondary path, whereas it becomes clear that any previous possible attempt at horizontal crack propagation has long been abandoned. Also, regeneration of a Mach cone along the incline can be observed, featuring a wider Mach cone angle, a sign of rupture deceleration. Finally, the sequence is completed at 96 μs with the rupture nearly exiting the field of view. Note the presence of secondary tensile microcracks along the main path, prior to its intersection with the bent path, and also along the entire length of the incline. Beyond the intersection point, the horizontal path still retains its virgin state, showing neither deformation, discontinuity, stress concentration, nor associated secondary tensile crack growth.

[26] The following case includes an incline angle of $\alpha = -80°$, shown in Figure 5. It is representative of the behavior of all cases that include inclined paths located on the extensional side, along an angle of large magnitude. Two sets of arrows are shown in each image, with the solid one indicating the position of the rupture along the horizontal path, and the broken arrow indicating the crack location along the incline. At 70 μs, it is evident that following the intersection point, both the horizontal and the inclined paths were triggered. Beyond the junction, the Mach cone is again present, carrying on apparently undisturbed from its state preceding the junction. It is attached to the tip of the rupture that is propagating along the horizontal line. It is noticeable also that the rupture tip lying along the horizontal path is at least twice farther removed from the junction than its counterpart that is following the inclined path. The subsequent frames are shown at times 78, 84, and 90 μs. The existence of the dual propagating path is consistent throughout all these frames, as is the delay experienced by the downward moving rupture when compared to the one moving horizontally. At every point in time, the Mach cone retains its connection to the horizontally moving rupture tip. Interestingly, in this case, the discontinuous edge of the Mach cone seems to be associated with the rupture traveling along the incline, as if driving it. However, this behavior cannot be asserted as being universal, since some other specimens tested with different angular inclinations and exhibiting features of a dual rupture do not always show an association between the Mach cone and the secondary rupture propagation. Finally, as the horizontal rupture prepares to exit the field of view in the last frame, the secondary rupture is still only halfway to reaching the equivalent point along its path, pointing to a deceleration factor nearing two in crack propagation between the two paths. Furthermore, beyond the junction, secondary tensile cracks are observed behind the rupture, below the interface of the main path, i.e., on the extensional side of the fault. Similar features are observed, again lagging the rupture, to

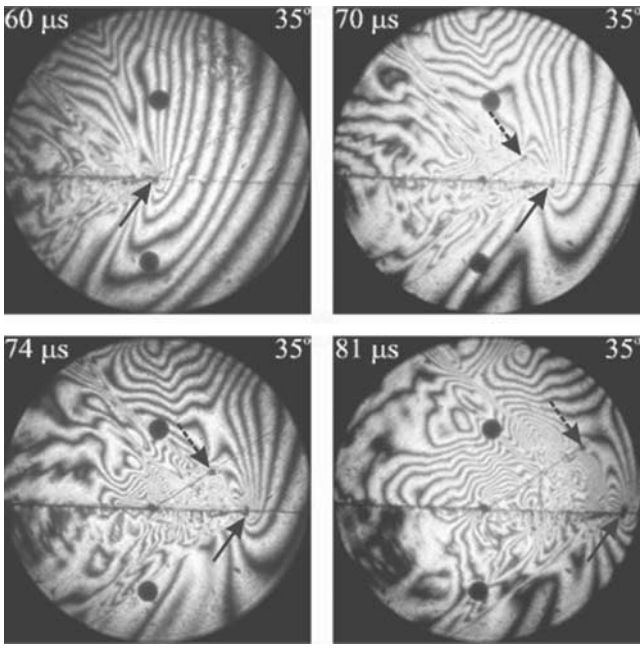

Figure 6. Isochromatic fringe pattern around a mode II crack propagating at supershear speed along a weak plane in Homalite-100. Beyond the junction with the extension of the horizontal path and a 35° incline, the crack simultaneously propagates along both paths. Times after impact are 60 μs, 70 μs, 74 μs, and 81 μs. Arrows indicate location of rupture tip.

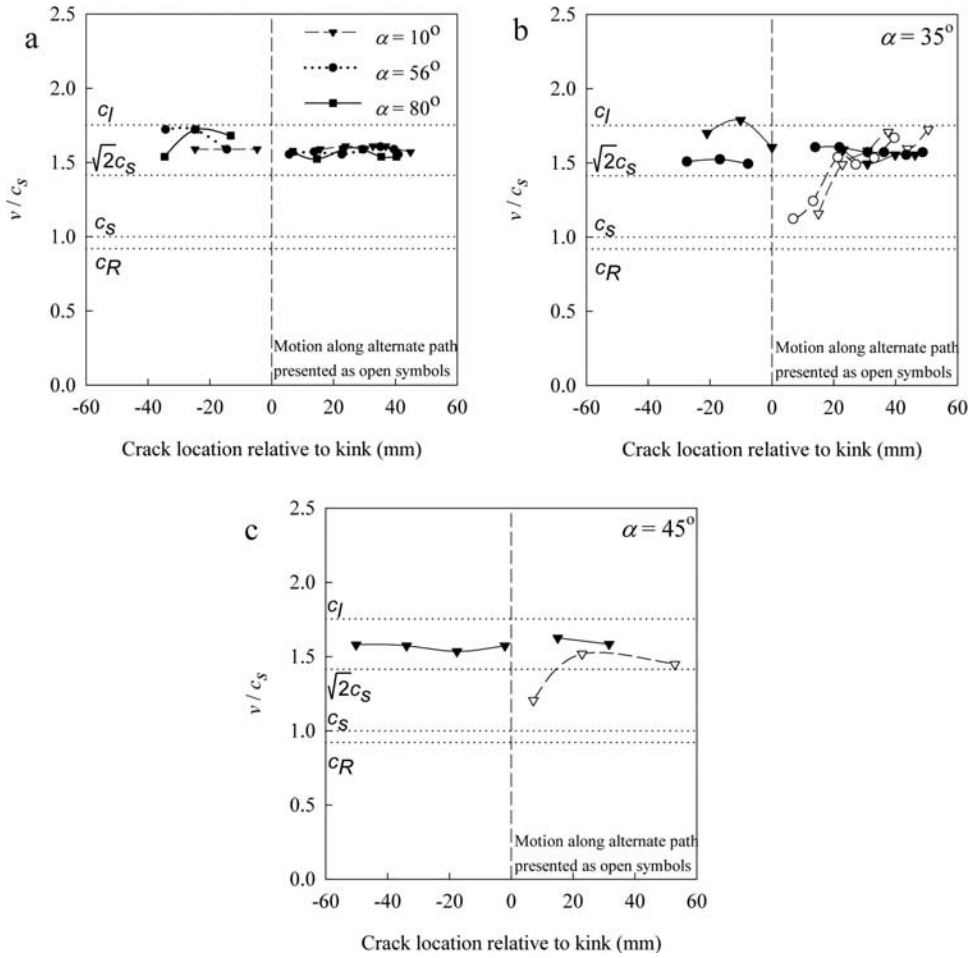

Figure 7. Speed history for a crack propagating in mode II along an extended weak plane, in the supershear regime, and encountering a secondary branch along its path. (a) A specimen having a secondary path inclined 10°, 56°, and 80° toward its compressional side. (b) A specimen having a secondary path inclined 35° toward its compressional side. (c) An angular incline of 45°. The following inclines are toward the extensional side of the specimens: (d) −10°, (e) −35°, (f) −45°, (g) −56°, (h) −80°, and (i) −100°.

the right of the interface of the secondary path. The presence of secondary microcracks positioned to the right of the incline indicates this side to be the extensional side and hence a change in stress state along that path, leading to a switch from right lateral to left lateral slip.

[27] Figure 6 illustrates another significant case of dual propagation, this time with the incline situated on the compressional side of the main fault (α = 35°). As before, the fringes display a steady, undisturbed evolution of the rupture along the horizontal path, beyond the junction. Unlike previous instances of dual rupture, advance along the incline, in the present case, not only remains supershear but also steadily accelerates. The presence of a Mach cone associated with that secondary supershear rupture is, however, very difficult if not at times impossible to visualize. This possibly arises from the fact that the secondary rupture is progressing within the shadow of the Mach cone associated with rupture motion along the main path. Figure 15 of *Templeton et al.* [2009] provides additional evidence of the existence of such a Mach cone intercepting the 35° path very close to the location of the secondary rupture tip. Indeed its presence is also corroborated by the rupture velocity measurements presented in the following sections.

[28] The presentation of these four sets of experiments was aimed at highlighting four distinct types of recurring behaviors that were observed. These qualitative assessments, based on fringe formation, have also been consistently reproduced by the numerical analysis presented by *Templeton et al.* [2009]. They are hereby followed by a more quantitative evaluation featuring speed evolution of the rupture for the various cases examined.

5. Experimental Observations: Quantitative Assessment

[29] Attention will first be placed on shear ruptures that initially propagate in the supershear regime. The review of these results will proceed primarily on the basis of whether the rupture is capable of extending itself, along either the horizontal or the inclined faults, beyond the junction. In addition, detailed records of the rupture velocity along these various paths will be presented.

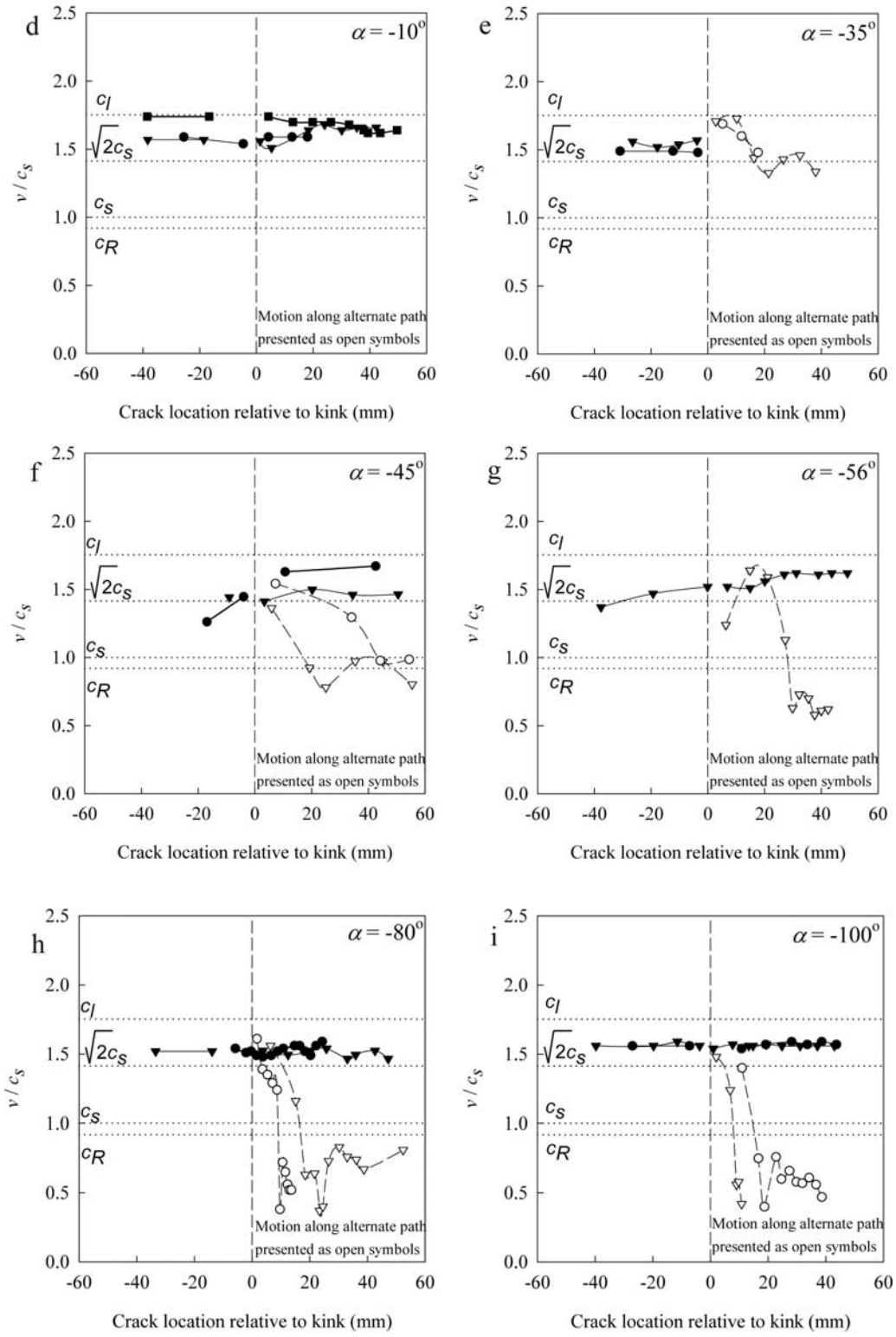

Figure 7. (continued)

5.1. Supershear Cases

[30] The first records to be examined correspond to the set of frames shown in Figure 3, and though not the result of the same mechanism, are combined with those having similar outcomes. Indeed, for occurrences where the secondary paths are located on the compressional side of the specimen (above the horizontal interface), and are either very shallow or have a large angular inclination, these secondary paths were bypassed, and the rupture proceeded solely along the extension of the horizontal, main path. This behavior is plotted in Figure 7a and is common to secondary incline angles α = 10°, 56°, and 80°. As already previewed

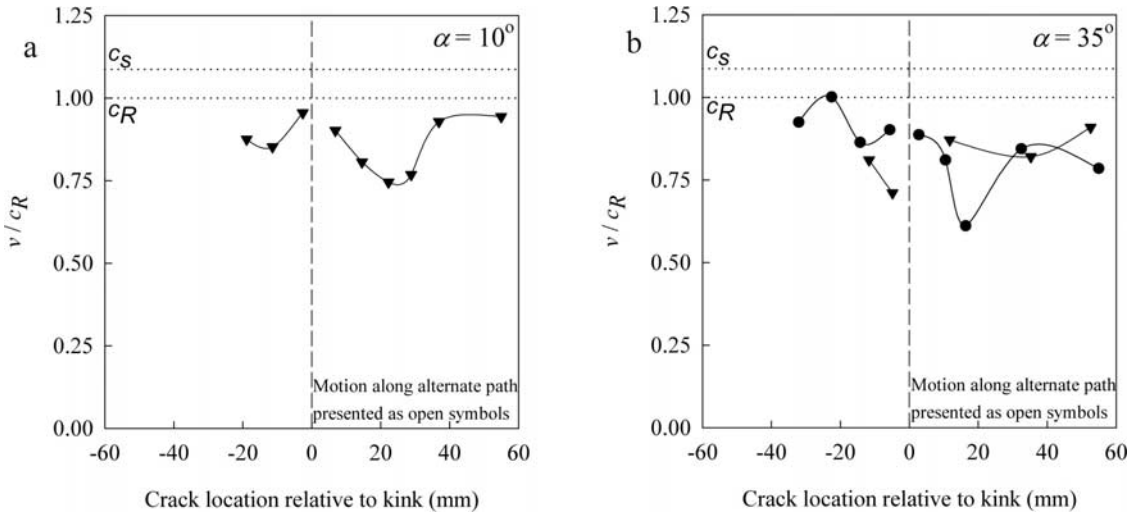

Figure 8. Speed history for a crack propagating in mode II along an extended weak plane, in the sub-Rayleigh regime, and encountering a secondary branch along its path. Specimens having a secondary path inclined (a) 10° and (b) 35° toward the compressional side. The following inclines are toward the extensional side of the specimens: (c) −10°, (d) −35°, (e) −56°, (f) −80°, and (g) −100°.

in the interferogram records, the velocity record reveals that the rupture crosses over the junction without exhibiting any sign of having been disturbed and seemingly without having acquired knowledge of the existence of the incline. Indeed, the rupture velocity having reached steady state prior to the intersection retains the said level throughout the entire area of interest. However, as indicated earlier, different mechanisms are liable to influence the behaviors for low inclination angles, on the one hand, and large inclination angles, on the other hand. Here it must be noted parenthetically that even for cases where no extension beyond the junction is available to the horizontal path, (bend geometry) an incoming supershear rupture is unable to branch unto a provided weakened incline of $\alpha > 50°$, and displays strong hesitations for any incline angles above 40° [*Rousseau and Rosakis*, 2003].

[31] Figure 7b shows the velocity history for a specimen with the secondary path inclined 35° toward the compressional side of the specimen. Figure 7b features two different attempts conducted on identical specimens. From these, where near superimposition of the various data points is evident, and similar cases in Figures 7 and 8, ample validation of the repeatability of these experiments is provided. As before, the motion along the horizontal path suffers no hesitation arising from the presence of the bend. However, a rupture does initiate along the incline, but its velocity initially undergoes a sharp drop upon jumping onto the incline to a level nearing c_s. Nevertheless, it soon recovers, and eventually, reaches c_l in the last available frame. The trend is clearly upward, strongly suggesting the transcendence of that level at later times. This is a unique behavior since, for all other configurations consisting of dual paths beyond the junction, the rupture generally decelerates continuously after reaching the branch. The acquisition of the requisite energy for such a unique performance must be interpreted in the context of the stress field generated by the main rupture propagating along the horizontal path. Figure 6 provides a clue, since the inclined rupture growth appears to be sustained by the jump in shear stresses associated with the Mach cone propagating along the main path. Indeed, in the presence of such a severe loading environment even higher rupture velocity levels, thus far not observed in nature, may nevertheless be in the realm of possibilities. It should be noted that the companion numerical analysis by *Templeton et al.* [2009] also reports secondary path rupture tips approaching or even exceeding the P wave speed of the material.

[32] The next case, illustrated in Figure 7c, represents the rupture velocity history, with a secondary path inclined 45° toward the compressional side of the specimen. Its behavior is very similar to that with the previous angular inclination, featuring an immediate deceleration, as the rupture jumps onto the incline, followed by a recovery to the stable [*Rosakis*, 2002] supershear speed of $\sqrt{2}c_s$. As discussed by *Rosakis* [2002, and references therein], both slip-weakening and velocity-weakening steady state models predict the existence of a stable supershear velocity range which starts at just above $\sqrt{2}c_s$ (the exact value of its lower bound depending on interface strength) and ends at c_l. Simultaneously, the rupture continues along the extension of the horizontal path, at the same rate as that along the prejunction fault.

[33] The subsequent plots (Figures 7d–7i) focus on the cases of dual paths beyond the junction, with the secondary path inclined clockwise, toward the extensional side of the specimens. The case of a secondary incline at a shallow angle of −10° offers no discernible variation from its counterpart having an upward bound secondary path. As seen in Figure 7d, for three separate tests conducted with identical specimens, the rupture velocity remains constant beyond the junction and moves past the secondary path as if it had been absent. Also, there is no optical evidence to indicate any initial attempt of the rupture at engaging unto the secondary path.

[34] As the incline angle increases to −35°, three novel behaviors are detected. First, growth along the horizontal path comes to an abrupt end, as indicated by the solid symbols of Figure 7e. Second, rupture propagation does

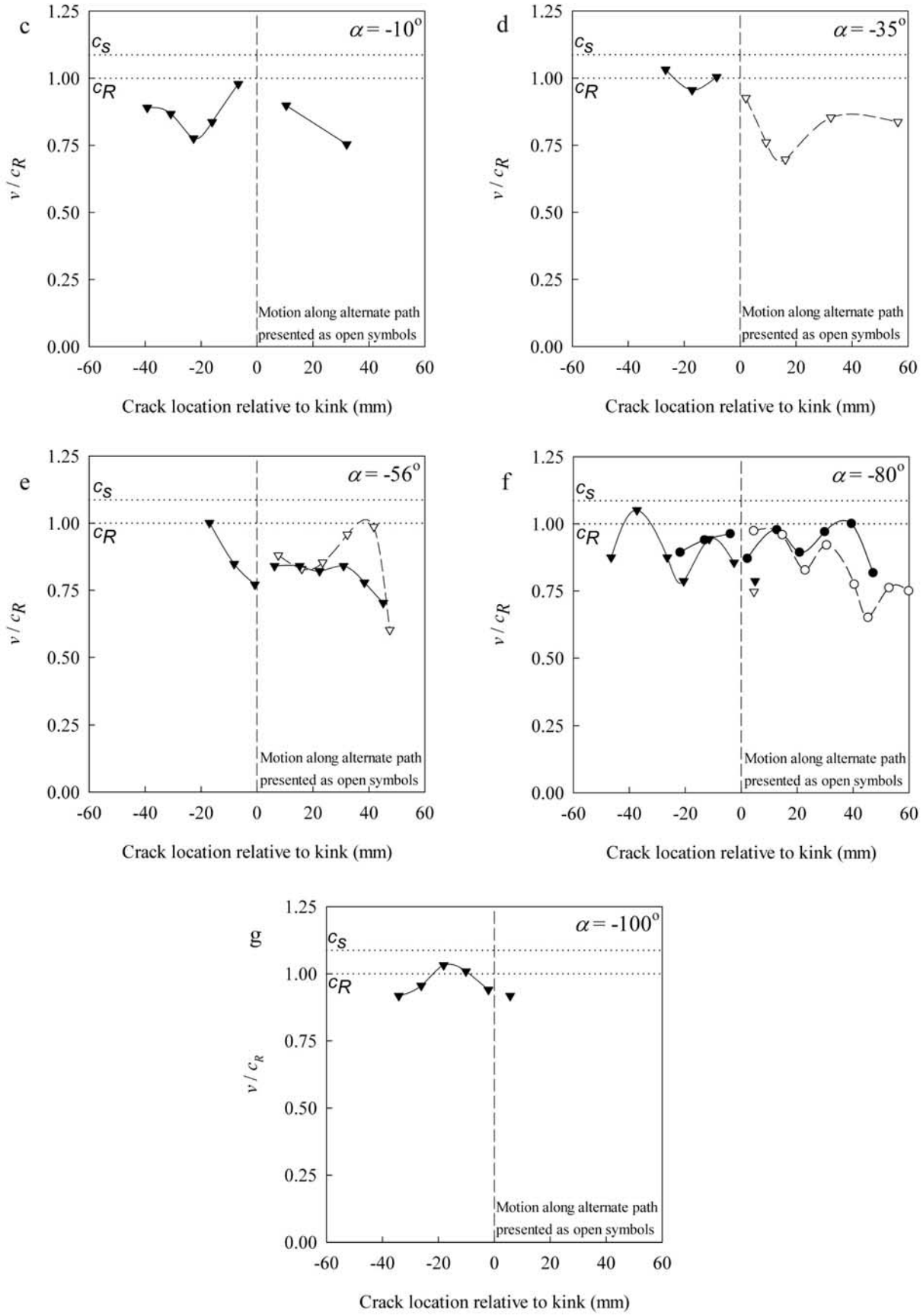

Figure 8. (continued)

resume its horizontal extension beyond the junction, but this time along the inclined path (seen as open symbols in Figure 7e). Third, there is a change in rupture velocity after the junction, as the crack instantly jumps to a value near c_l. A brief stay at that level is followed by deceleration, until the crack again finds a steady state platform at $\sqrt{2}\ c_s$.

[35] Figure 7f presents the experimental data for an incline angle of $-45°$. It features simultaneous progressions along both paths, beyond the junction, wherein the velocity remains constant along the horizontal branch. A turn unto the incline at constant velocity relative to the prejunction level is followed by a monotonic and slow deceleration to c_R.

[36] The next case tested includes a secondary path inclined at an angle $\alpha = -56°$, again accompanied by the continuation of horizontal propagation beyond the junction. Here again, along the main, horizontal interface, crack progression past the point common to all three paths remains unaltered (Figure 7g). The velocity history does not show any evidence of the rupture having encountered a crossroad. However, simultaneously, a crack is also initiated along the incline. In this case, an initial drop in crack velocity relative to the incoming rupture velocity is registered. A sudden acceleration, then a deceleration are observed, down to sub-Rayleigh levels, where the crack velocity lingers. There exists therefore a large gap in crack progression along the two paths. Indeed, features of the fringe records show the crack having reached the boundaries of the field of view when following the extension of the main path, while the crack moving along secondary path is but halfway in its evolution toward the circumference of the field of view.

[37] The behavior for the case of dual paths, with the secondary fault oriented $-80°$ toward the extensional side is similar to the previous one. Indeed, the incoming rupture triggers debonding of both possible routes. Again, motion along the extension of the main path seems to be unaltered. As seen in Figure 7h, crack velocity remains constant, and at the same level as that prior to the junction. Along the incline, rapid deceleration ensues, to a constant sub-Rayleigh level. The same pattern is repeated almost identically for the case of a secondary incline at $\alpha = -100°$ (Figure 7i). This last case is rather surprising, since intuitively it would seem difficult for the incoming rupture to provide enough energy to permit continued progress of the supershear rupture at a constant level, while simultaneously triggering a secondary path that essentially allows the rupture to take an abrupt turn toward the direction from which it came.

5.2. Sub-Rayleigh Cases

[38] Figures 8a and 8b show the results of experiments conducted, with the secondary fault located at angles of $10°$ and $35°$ toward the compressional side of the specimen. Both show continued progress along the extension of the horizontal fault, whereas the incline plane is not triggered. Also attempted, were cases that include angular inclination of $56°$ and $80°$, for which unfortunately no optical record could be obtained. However, postmortem analysis of these specimens does indicate a behavior identical to that of the two previous specimens. It is noted also that the velocity record is not as smooth at those of the supershear cases partly because these were determined by visually locating the crack tip (as opposed to using the more robust Mach cone angle, in the supershear cases), and also partly due to the instabilities inherent to the sub-Rayleigh regime. The discussions to follow refer to secondary path inclined downward, toward the extensional side of the specimens.

[39] Figure 8c displays the data for the shallow angle of $-10°$. It is no different from the results obtained in the supershear case, where the progression of the rupture is limited solely to the horizontal path, seemingly unaware of the presence of the very shallow incline. For the larger angular inclination of $-35°$ (Figure 8d), the opposite does happen. As in the supershear case, the extension of the horizontal path is bypassed, and only the inclined fault is triggered. The continued progression within the secondary path is marked by a slight deceleration.

[40] In light of these results, it is noteworthy to cite the 1979 Imperial Valley earthquake rupture, which has been thought to have occurred at sub-Rayleigh speeds. The Imperial Valley fault is oriented roughly north-northwest, and is bisected by the Brawley fault which has a north-south bearing [*Archuleta*, 1984]. The angle between the two faults is thought to be nearly $-34°$, with the latter positioned within the extensional side of the former. The strike-slip earthquake, having initiated along the Imperial Valley fault in a right lateral slip, veered onto the Brawley fault, again in a right lateral motion, completely circumventing the remainder of the Imperial Valley fault [*Archuleta*, 1984]. The detailed far-field conditions pertaining to this earthquake differ from those studied in the present experiments. However, it is very encouraging to observe a natural event exhibiting features very similar to an idealized laboratory experiment of similar fault geometry.

[41] For $\alpha = -56°$ (Figure 8e), dual progression along the two alternate planes is resumed. Whereas for the most part the velocity along the horizontal path remains constant, a slight acceleration is experienced along the incline, allowing the rupture to progress at a faster rate along it. The last of the series, Figure 8f, shows the velocity history corresponding to an inclination of the secondary path of $-80°$, which features dual triggering with gradual deceleration along the incline. Finally, note that unlike the previously mentioned supershear case featuring a dual path with an incline of $-100°$, and unlike a sub-Rayleigh case featuring only the single $-100°$ bend [see *Rousseau and Rosakis*, 2003], for which cases the inclines were always triggered, an experiment within the sub-Rayleigh range with dual paths and a $-100°$ incline could not provide the energy necessary to initiate a rupture along the incline (Figure 8g).

6. Experimental Observations: Discussions

[42] The propensity of the rupture to branch onto the secondary path is summarized in Table 1, where the relative speeds of the secondary ruptures are presented with respect to the speed of propagation of the main rupture, after the crossing of the junction. This is further expressed graphically in Figure 9, which shows the ratio of the rupture velocity along the incline, immediately following the junction, to the rupture velocity along the main horizontal path, immediately prior to the junction, for cases involving dual paths after the intersection point (open, inverted triangles). Thus, this represents the immediate response of the incline. Beyond

Table 1. Relative Progression of the Ruptures Beyond the Junction of a Weak Plane With Branched Paths

Angle	v_2/v_1
Supershear	
−100	0.50
−80	0.55
−56	0.70
−45	0.70
−35	N/A[a]
−10	0.00
10	0.00
35	0.85
45	0.70
56	0.00
80	0.00
Sub-Rayleigh	
−100	0.00
−80	0.90
−56	1.05
−35	N/A[a]
−10	0.00
10	0.00
35	0.00
56	0.00
80	0.00

[a]Only secondary fault activated; extension of primary fault remaining intact.

this, several other factors (e.g., static far-field conditions) may come into play with time and alter the rupture velocity. The speed ratio, in the immediate vicinity of the bend, is presented for cases where the incline angle is situated both on the extensional and on the compressional side of the specimens. Superimposed onto the plot are results from previous experiments performed by *Rousseau and Rosakis* [2003]. In those earlier experiments, the weakened path provided to the incoming rupture consisted of a main path turning into a kink or bend, with no further extension of the horizontal path made available (solid crosses). Note that for the current experiments, the response of the horizontal extension is not shown since, upon that continued path being triggered, its immediate velocity remains constant at a value equal to that of the incoming rupture.

[43] For the case of a simple bend, the dependence between postjunction velocity and bend angle can be directly attributed to a combination of the asymptotic crack tip stress field and friction, as formulated by the *Rousseau and Rosakis* [2003]. The formulation is an adaptation of the one presented by *Poliakov et al.* [2002] to account for the possibility of face opening. It is clear, from Figure 9, that cases that include dual paths after the junction, do not adhere to the previously formulated criterion, especially for shallow incline angles which cannot undergo rupturing simultaneously with the horizontal path. Furthermore, for the supershear cases (Figure 9a), the maximum triggering response of the dual path experiments occurs at or near −35°, and decreases with increasing magnitude of extensional angle. By contrast, cases consisting of a single bend were more responsive to the incoming shear crack with increasing extensional inclination. The dual path sub-Rayleigh cases (Figure 9b) distinguished themselves from their simple bend counterparts particularly when the incline is located on the compressional side of the specimen, for which cases, their triggering becomes impossible. Also, the extensional side response for the simple bend cases is nearly constant with angular inclination, whereas their dual path counterparts do exhibit some variations. For the dual path geometry, the main difference between the supershear and sub-Rayleigh results appears to be in the influence of the intersection of the shear shock waves, of the rupture propagating horizontally, on the stress state of the inclined plane. Here, and for certain angles of inclination, it is conceivable that the shear shock wave discontinuity line may trigger and drive a rupture along the inclined paths. This perhaps accounts for most of the differences between the experimental results reported for these sub-Rayleigh and the supershear cases, especially for bends located on the compressional side.

[44] An attempt at clarifying the long-term response of these inclined paths is presented in Figures 10a and 10b for supershear and sub-Rayleigh cases, respectively, in terms of the ratio of the average or mean rupture speed of a specimen, along the entire path under scrutiny, following and preceding the junction. On the extensional side, inverted trends between simple and dual paths appear to be the norm. Indeed, dual path cases exhibit a sharp drop in average velocity with increasing extensional angle, whereas apart from some

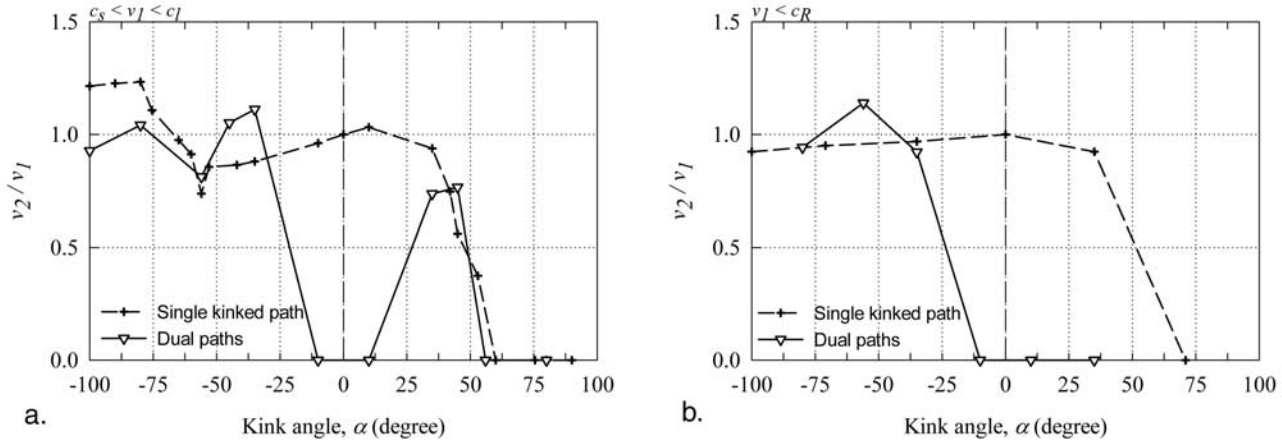

Figure 9. Crack speeds along fault bends of various inclinations for incoming (a) supershear and (b) sub-Rayleigh shear cracks in specimens with both single bends and dual branches. Crack speed along the secondary fault is normalized by the terminal crack speed of the primary plane.

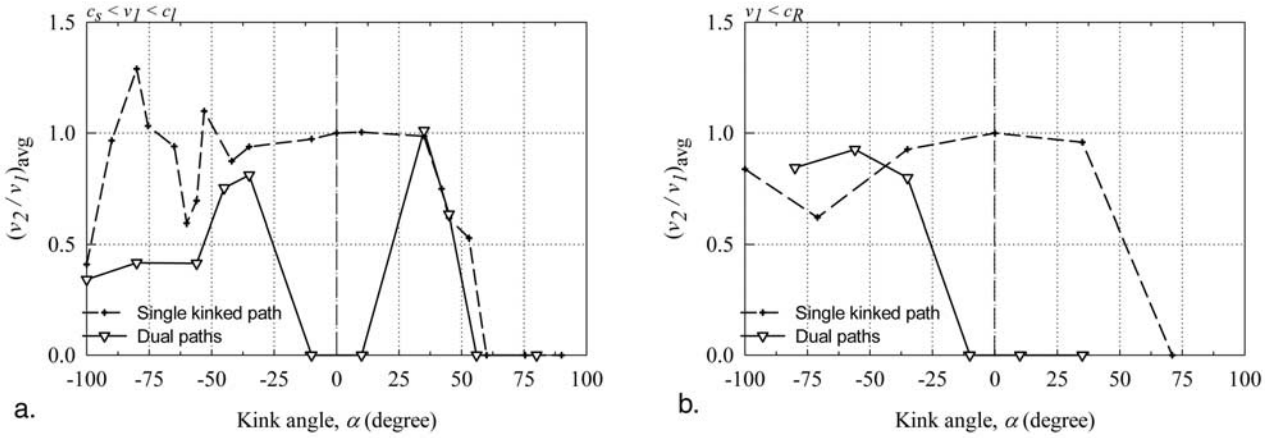

Figure 10. Average steady state crack speeds along fault bends of various inclinations for incoming (a) supershear and (b) sub-Rayleigh shear cracks in specimens with both single bends and dual branches. Steady state crack speed beyond the junction is normalized by the equivalent speed prior to the junction.

oscillations, the average velocities along the simple bends remain relatively constant with increasing inclination. In the sub-Rayleigh case, variations in behavior, due to the differences between the types of specimens, again appear to follow opposite extremes, with each type of specimen maintaining its systematic level of constant velocity.

7. Influence of the Impact-Generated Stress Field

[45] As the mode II rupture propagates along the path to which it is confined, it is also affected by existing stress fields, which are prevalent within the specimen [*Poliakov et al.*, 2002; *Bhat et al.*, 2004]. In the current case, these are generated by the indirect impact of the projectile against the edge of the specimen, through the metallic buffer, but are well established far before their arrival at the rupture. Since wave reflections from the specimen boundaries have not yet occurred at the time of kinking, this compressive prestate remains active and influences the kinking process. A compressive pulse is generated and propagates throughout the specimen. The appended metallic buffer being much stiffer than the Homalite specimen, the maximum intensity of the stress at the head of the compressive pulse can be approximated by

$$\sigma_{xx} = \frac{E}{1-\nu^2}\frac{V}{c_l} = \sigma_0 \tag{2}$$

where c_l is the longitudinal wave speed, and E is the Young's modulus of the polymer, and V is the velocity of the impactor. Using the properties of Homalite-100 given in a previous section, the generated stress field are estimated to reach a maximum of σ_o = 79 MPa for the supershear case (V = 30 m/s) and σ_o = 54 MPa for the subsonic case (V = 20 m/s).

[46] The same can also be verified independently from the photoelastic optical records (fringes), and equation (1). Using the necessary material properties and material constants, also provided in a previous section, result in σ_o = 71 MPa for the supershear case and σ_o = 49 MPa for the subsonic case. Both results agree extremely well with the previous estimates.

[47] Observing the fringes of, say, Figure 3 (top left), one notes that the incoming compressive stresses are not vertical, but rather exhibit a slight downward slant while journeying in the direction of crack motion (to the right in Figure 3 (top left)). On the basis of the profile of these fringes just before the rupture tip, the direction of principal stresses can be determined. These are illustrated graphically in Figure 11, which shows the principal direction of the compressive stresses acting simultaneously on the main fault and on secondary faults of different inclinations to the horizontal at the time corresponding to the arrival of the

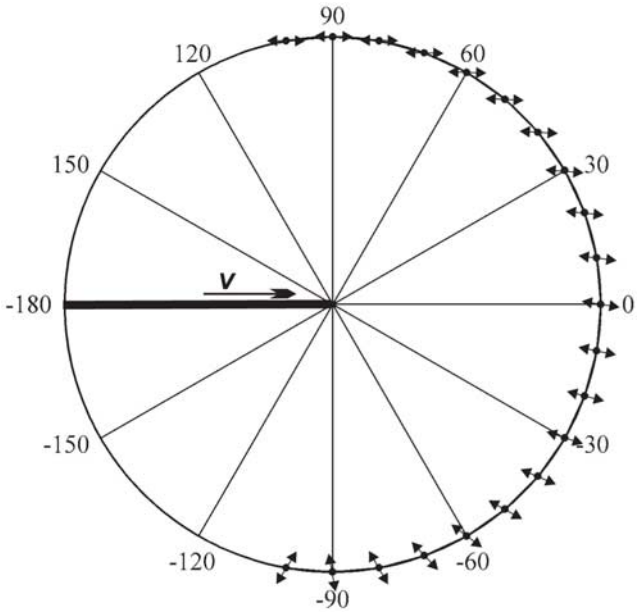

Figure 11. Schematic showing the principal directions of the impact-induced compressive stresses in the immediate neighborhood of a moving shear rupture as a function of fault inclination.

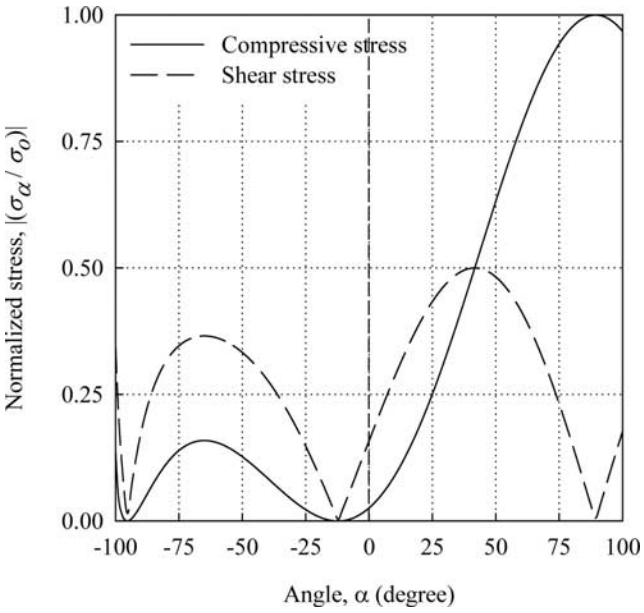

Figure 12. Compressive and shear stresses acting perpendicularly and parallel to a fault interface, respectively.

crack tip at the branch. This information is provided for angular orientations ranging from $-100°$ to $100°$, and is valid for both supershear and sub-Rayleigh cases. These principal stresses are further resolved into compressive stresses perpendicular to a fault branch of arbitrary inclination, and shear stress in the direction of the said branch. These two stress components are plotted simultaneously in Figure 12. The stresses normalized by the maximum compressive stress, σ_o, experienced by the specimen, such that for instance, a compressive stress value of unity, also corresponding to shear stress value of zero, near a fault inclination of $90°$, does correspond to the principal stresses being oriented perpendicularly to that direction. It is particularly noticeable that the compressive stresses are predominantly high on the compressional side of the specimen, while barely registering a maximum of 20% of the value of the head of the compressive pulse, on the extensional side. This certainly establishes a discouraging environment for active rupture on the former side of the specimen, in comparison to the latter.

8. Concluding Remarks

[48] Earlier experiments conducted by *Rousseau and Rosakis* [2003] represent the initial attempt to reproduce in the laboratory conditions prevalent during earthquake ruptures in the presence of fault complexities. These featured an initially straight path later veering onto a single bend of arbitrary angular inclination. The conditions surrounding these earlier experiments were reproduced here, with the appendage of the additional complexity of dual branches, thereby giving the propagating fault the possibility of election between arrest, simultaneous continuation along both branches, or a choice between either one of the two available paths. Similarities and differences pertaining to the two respective types of specimens are highlighted. In particular, as compared to the former, the branched specimens only featured secondary rupture propagation over a narrow range of angular inclination and has been numerically validated by *Templeton et al.* [2009]. Except for an inclination of $-35°$, the secondary branches never interfered with continued propagation along the main, horizontal path. Also, various responses are noted between cases featuring sub-Rayleigh and supershear rupture propagation, with the latter being more prone to accommodate propagation than the former. Furthermore, for supershear cases, a noteworthy behavior manifests itself (both in experiments and numerical simulations by *Templeton et al.* [2009]) in the remarkable phenomenon of the discontinuity of the Mach cone attached to the main (horizontal) branch acting as a trigger and driving force to the propagation along an adjacent secondary surface, (e.g., $\alpha = +35°$) driving it in certain cases toward the longitudinal wave speed of the material.

[49] **Acknowledgments.** The authors were supported by U.S. DOE grant DE-FG52-06NA 26209, NSF-EAR grant EAR-0711545, and ONR MURI grant N0014-06-1-0730. Many helpful discussions with James Rice, Renata Dmowska, Harsha Bhat, and Elizabeth Templeton of Harvard University are also acknowledged.

References

Aagaard, B. T., and T. H. Heaton (2004), Near-source ground motions from simulations of sustained intersonic and supersonic fault ruptures, *Bull. Seismol. Soc. Am.*, *94*(6), 2064–2078, doi:10.1785/0120030249.

Aki, K. (1979), Characterization of barriers on an earthquake fault, *J. Geophys. Res.*, *84*, 6140–6148, doi:10.1029/JB084iB11p06140.

Ando, R., and T. Yamashita (2007), Effects of mesoscopic-scale fault structure on dynamic earthquake ruptures: Dynamic formation of geometrical complexity of earthquake faults, *J. Geophys. Res.*, *112*, B09303, doi:10.1029/2006JB004612.

Aochi, H., E. Fukuyama, and M. Matsu'ura (2000), Spontaneous rupture propagation on a non-planar fault in 3-D elastic medium, *Pure Appl. Geophys.*, *157*(11–12), 2003–2027, doi:10.1007/PL00001072.

Archuleta, R. J. (1984), A faulting model for the 1979 Imperial Valley earthquake, *J. Geophys. Res.*, *89*, 4559–4585, doi:10.1029/JB089iB06p04559.

Barka, A. A., and K. Kadinsky-Cade (1988), Strike-slip fault geometry in Turkey and its influence on earthquake activity, *Tectonics*, *7*, 663–684, doi:10.1029/TC007i003p00663.

Bhat, H. S., R. Dmowska, J. R. Rice, and N. Kame (2004), Dynamic slip transfer from the Denali to Totschunda faults, Alaska: Testing theory for fault branching, *Bull. Seismol. Soc. Am.*, *94*(6B), S202–S213, doi:10.1785/0120040601.

Bhat, H. S., M. Olives, R. Dmowska, and J. R. Rice (2007), Role of fault branches in earthquake rupture dynamics, *J. Geophys. Res.*, *112*, B11309, doi:10.1029/2007JB005027.

Biegel, R. L., C. G. Sammis, and A. J. Rosakis (2007), Interaction of a dynamic rupture on a fault plane with short frictionless fault branches, *Pure Appl. Geophys.*, *164*(10), 1881–1904, doi:10.1007/s00024-007-0251-2.

Bouchon, M., and H. Karabulut (2008), The aftershock signature of supershear earthquakes, *Science*, *320*(5881), 1323–1325, doi:10.1126/science.1155030.

Bouchon, M., and M. Vallée (2003), Observation of long supershear rupture during the magnitude 8.1 Kunlunshan earthquake, *Science*, *301*(5634), 824–826, doi:10.1126/science.1086832.

Bouchon, M., N. Toksöz, H. Karabulut, M. Bouin, M. Dietrich, M. Aktar, M. Edie, and A. Mustafa (2000), Seismic imaging of the 1999 Izmit (Turkey) rupture inferred from the near-fault recordings, *Geophys. Res. Lett.*, *27*(18), 3013–3016, doi:10.1029/2000GL011761.

Bouchon, M., M. P. Bouin, H. Karabulut, M. N. Toksöz, M. Dietrich, and A. J. Rosakis (2001), How fast is rupture during an earthquake? New insights from the 1999 Turkey earthquakes, *Geophys. Res. Lett.*, *28*(14), 2723–2726, doi:10.1029/2001GL013112.

Burridge, R., G. Conn, and L. B. Freund (1979), The stability of a rapid mode II crack with finite cohesive traction, *J. Geophys. Res.*, *84*(B5), 2210–2222, doi:10.1029/JB084iB05p02210.

Dally, J. W., and W. F. Riley (1991), *Experimental Stress Analysis*, McGraw-Hill, New York.

Duan, B., and D. D. Oglesby (2005), Multicycle dynamics of nonplanar strike-slip faults, *J. Geophys. Res.*, *110*, B03304, doi:10.1029/2004JB003298.

Duan, B., and D. D. Oglesby (2007), Nonuniform prestress from prior earthquakes and the effect on dynamics of branched fault systems, *J. Geophys. Res.*, *112*, B05308, doi:10.1029/2006JB004443.

Dunham, E. M., and R. J. Archuleta (2004), Evidence for a supershear transient during the 2002 Denali fault earthquake, *Bull. Seismol. Soc. Am.*, *94*(6B), S256–S268, doi:10.1785/0120040616.

Ellsworth, W. L., M. Celebi, J. R. Evans, E. G. Jensen, R. Kayen, M. C. Metz, D. J. Nyman, J. W. Roddick, P. Spudich, and C. D. Stephens (2004), Near-field ground motion of the 2002 Denali fault, Alaska, earthquake recorded at pump station 10, *Earthq. Spectra*, *20*(3), 597–615, doi:10.1193/1.1778172.

Fliss, S., H. S. Bhat, R. Dmowska, and J. R. Rice (2005), Fault branching and rupture directivity, *J. Geophys. Res.*, *110*, B06312, doi:10.1029/2004JB003368.

Harris, R. A., and S. M. Day (1993), Dynamics of fault interaction: Parallel strike-slip faults, *J. Geophys. Res.*, *98*(B3), 4461–4472.

Harris, R. A., and S. M. Day (1999), Dynamic 3D simulations of earthquakes on en echelon faults, *J. Geophys. Res.*, *26*(14), 2089–2092.

Harris, R. A., R. J. Archuleta, and S. M. Day (1991), Fault steps and the dynamic rupture process: 2-D numerical simulations of a spontaneously propagating shear fracture, *Geophys. Res. Lett.*, *18*, 893–896, doi:10.1029/91GL01061.

Harris, R. A., J. F. Dolan, R. Hartleb, and S. M. Day (2002), The 1999 Izmit, Turkey, earthquake: A 3D dynamic stress transfer model of intra earthquake triggering, *Bull. Seismol. Soc. Am.*, *92*(1), 245–255, doi:10.1785/0120000825.

Husseini, M. I., D. B. Jovanovich, M. J. Randall, and L. B. Freund (1975), The fracture energy of earthquakes, *Geophys. J. R. Astron. Soc.*, *43*, 367–385.

Ji, C., D. V. Helmberger, and D. J. Wald (2000), Basic structure estimation by waveform modeling: Forward and inverse methods, *Bull. Seismol. Soc. Am.*, *90*(4), 964–976, doi:10.1785/0119990080.

Kame, N., J. R. Rice, and R. Dmowska (2003), Effects of prestress state and rupture velocity on dynamic fault branching, *J. Geophys. Res.*, *108*(B5), 2265, doi:10.1029/2002JB002189.

Kanamori, H. (1994), Mechanics of earthquakes, *Annu. Rev. Earth Planet. Sci.*, *22*, 207–237, doi:10.1146/annurev.ea.22.050194.001231.

King, G. C. P., and J. Nabelek (1985), Role of fault bends in the initiation and termination of earthquake rupture, *Science*, *228*(4702), 984–987, doi:10.1126/science.228.4702.984.

Poliakov, A. N. B., R. Dmowska, and J. R. Rice (2002), Dynamic shear rupture interactions with fault bends and off-axis secondary faulting, *J. Geophys. Res.*, *107*(B11), 2295, doi:10.1029/2001JB000572.

Rice, J. R. (1980), The mechanics of earthquake rupture in *Physics of the Earth's Interior*, edited by A. M. Dziewonski and E. Boschi, pp. 555–649, North Holland, Amsterdam.

Rice, J. R. (2001), New perspectives on crack and fault dynamics in *Mechanics for a New Millennium: Proceedings of the 20th International Congress of Theoretical and Applied Mechanics, 20 Aug–2 Sept 2001, Chicago*, edited by H. Aref and J. W. Phillips, pp. 1–23, Kluwer Acad, New York.

Robinson, D. P., C. Brough, and S. Das (2006), The M_w 7.8, 2001 Kunlunshan earthquake: Extreme rupture speed variability and effect of fault geometry, *J. Geophys. Res.*, *111*, B08303, doi:10.1029/2005JB004137.

Rosakis, A. J. (2002), Intersonic shear cracks and fault ruptures, *Adv. Phys.*, *51*(4), 1189–1257, doi:10.1080/00018730210122328.

Rosakis, A. J., O. Samudrala, and D. Coker (1999), Cracks faster than the shear wave speed, *Science*, *284*, 1337–1340, doi:10.1126/science.284.5418.1337.

Rosakis, A. J., G. Lykotrafitis, H. Kanamori, and K. Xia (2007), Speeds, directionality and modes in *Treatise on Geophysics*, vol. 4, edited by G. Schubert, pp. 151–192, Elsevier, Amsterdam.

Rousseau, C.-E., and A. J. Rosakis (2003), On the influence of fault bends on the growth of sub-Rayleigh and intersonic dynamic shear ruptures, *J. Geophys. Res.*, *108*(B9), 2411, doi:10.1029/2002JB002310.

Samudrala, O., Y. Y. Huang, and A. J. Rosakis (2002), Subsonic and intersonic mode II crack propagation with a rate-dependent cohesive zone, *J. Mech. Phys. Solids*, *50*, 1231–1268, doi:10.1016/S0022-5096(01)00129-6.

Segall, P., and Y. Du (1993), How similar were the 1934 and 1966 Parkfield earthquakes?, *J. Geophys. Res.*, *98*(B3), 4527–4539, doi:10.1029/92JB02408.

Segall, P., and D. D. Pollard (1980), Mechanics of discontinuous faults, *J. Geophys. Res.*, *85*, 4337–4350, doi:10.1029/JB085iB08p04337.

Sibson, R. H. (1985), Stopping of earthquake ruptures at dilatational fault jogs, *Nature*, *316*, 248–251, doi:10.1038/316248a0.

Sibson, R. H. (1986), Rupture interactions with fault jogs in *Earthquake Source Mechanics*, *Geophys. Monogr. Ser.*, vol. *37*, edited by S. Das et al., pp. 157–167, AGU, Washington, D. C.

Sowers, J. M., J. R. Unruh, W. R. Lettis, and T. D. Rubin (1994), Relationship of the Kickapoo fault to the Johnson Valley and Homestead Valley faults, San Bernardino County, California, *Bull. Seismol. Soc. Am.*, *84*, 528–536.

Spudich, P., and E. Cranswick (1984), Direct observation of rupture propagation during the 1979 Imperial Valley earthquake using a short baseline accelerometer array, *Bull. Seismol. Soc. Am.*, *74*(6), 2083–2114.

Templeton, E. L., A. Baudet, H. S. Bhat, R. Dmowska, J. R. Rice, A. J. Rosakis, and C-.E. Rousseau (2009), Finite element simulations of dynamic shear rupture experiments and dynamic path selection along kinked and branched faults, *J. Geophys. Res.*, *114*, B08304, doi:10.1029/2008JB006174.

Vallée, M., M. Landès, N. M. Shapiro, and Y. Klinger (2008), The 14 November 2001 Kokoxili (Tibet) earthquake: High-frequency seismic radiation originating from the transitions between sub-Rayleigh and supershear rupture velocity regimes, *J. Geophys. Res.*, *113*, B07305, doi:10.1029/2007JB005520.

Wald, D. J., and T. H. Heaton (1994), Spatial and temporal distribution of slip for the 1992 Landers, California, earthquake, *Bull. Seismol. Soc. Am.*, *84*, 668–691.

Wallace, R. E. (1970), Earthquake recurrence intervals of the San Andreas fault, *Geol. Soc. Am. Bull.*, *81*, 2875–2890, doi:10.1130/0016-7606(1970)81[2875:ERIOTS]2.0.CO;2.

Xia, K., A. J. Rosakis, and H. Kanamori (2004), Laboratory earthquakes: The sub-Rayleigh-to-supershear rupture transition, *Science*, *303*(5665), 1859–1861, doi:10.1126/science.1094022.

Xia, K., A. J. Rosakis, and H. Kanamori (2005), Supershear and subrayleigh to supershear transition observed in laboratory earthquake experiments, *Exp. Tech.*, *29*(3), 63–66, doi:10.1111/j.1747-1567.2005.tb00220.x.

Zachariasen, J., and K. Sieh (1995), The transfer of slip between two en echelon strike-slip faults: A case study from the 1992 Landers earthquake, southern California, *J. Geophys. Res.*, *100*, 15,281–15,301, doi:10.1029/95JB00918.

A. J. Rosakis, Graduate Aeronautical Laboratories, California Institute of Technology, Pasadena, CA 91125, USA. (rosakis@aero.caltech.edu)

C.-E. Rousseau, Department of Mechanical Engineering, University of Rhode Island, Kingston, RI 02881, USA. (rousseau@uri.edu)